Cell Reports
Physical Science

CellPress
OPEN ACCESS

Article

Molecular understanding of interphase formation via *operando* polymerization on lithium metal anode

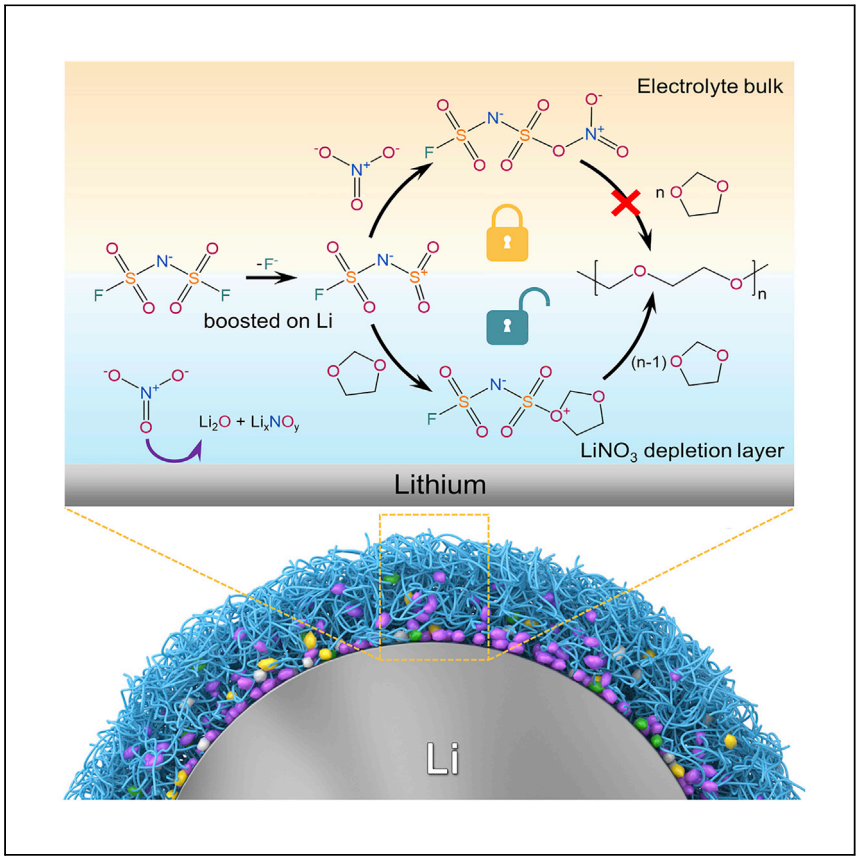

The molecular understanding of the formation and evolution mechanism of the polymeric-inorganic SEI formation sheds light on the elusive dynamic processes of the interphase. Jie et al use this analysis to develop the rational design of SEI for practical Li metal batteries.

Yulin Jie, Yaolin Xu, Yawei Chen, ..., Tao Cheng, Kang Xu, Shuhong Jiao

yan.lu@helmholtz-berlin.de (Y.L.)
tcheng@suda.edu.cn (T.C.)
conrad.k.xu.civ@mail.mil (K.X.)
jiaosh@ustc.edu.cn (S.J.)

Highlights

A polymeric-inorganic SEI is formed via interphase-confined *operando* polymerization

The SEI accommodates Li^0-growth by 100 times through stretching and self-healing

Conformal interphase facilitates homogeneous Li^+ transport and columnar Li deposition

Jie et al., Cell Reports Physical Science 3, 101057
October 19, 2022
https://doi.org/10.1016/j.xcrp.2022.101057

Cell Reports
Physical Science

CellPress
OPEN ACCESS

Article

Molecular understanding of interphase formation via *operando* polymerization on lithium metal anode

Yulin Jie,[1,12] Yaolin Xu,[2,12] Yawei Chen,[1,12] Miao Xie,[3,12] Yue Liu,[3] Fanyang Huang,[1] Zdravko Kochovski,[2] Zhanwu Lei,[1] Lei Zheng,[4,5] Pengduo Song,[6] Chuansheng Hu,[7] Zeming Qi,[7] Xinpeng Li,[1] Shiyang Wang,[1] Yanbin Shen,[5] Liwei Chen,[5,8] Yezi You,[6] Xiaodi Ren,[1] William A. Goddard III,[9] Ruiguo Cao,[1] Yan Lu,[2,10,*] Tao Cheng,[3,*] Kang Xu,[11,*] and Shuhong Jiao[1,13,*]

SUMMARY

The stable cycling of lithium electrode has been significantly impeded by the lack of comprehensive and in-depth understanding of the complicated chemistry and unclear formation/evolution mechanisms of solid-electrolyte interphase (SEI). Here we report the formation mechanism of an *operando* polymerized SEI at the Li/electrolyte interface in an ether electrolyte and its dynamic evolution during the lithium growth process. The polymerization process is initiated by the consumption of the polymerization inhibitor $LiNO_3$ with the formation of inorganic lithium salts at the Li-electrolyte interface, followed by instantaneous ring-opening polymerization of the cyclic ether solvent triggered by the initiator $FSO_2NSO_2\cdot$ radical, leading to the formation of a polymeric-inorganic composite SEI. The resulted SEI exhibits excellent mechanical flexibility and self-healing property that can effectively accommodate more than 100 times' swelling of lithium during growth by stretching and thinning itself from ~100 nm to 7 nm, achieving an ultrahigh Coulombic efficiency (99.73%) for lithium plating/stripping.

INTRODUCTION

Metallic lithium (Li^0) holds great promise as the ultimate anode for Li-based batteries because of the combination of an extremely high theoretical capacity (~3,860 mAh g^{-1}) and the lowest working potential (−3.040 V versus standard hydrogen electrode).[1,2] However, its practical implementation has been plagued by the poor Coulombic efficiency (CE) and notorious dendrite growth in the Li plating/stripping processes during battery operation, which is strongly correlated with the unstable and fragile nature of the solid-electrolyte interphase (SEI) formed on Li deposits.[3–8] The SEI has been considered as "the most important but the least understood" component in Li-based batteries,[9] due to the complexity and dynamic evolution of its composition and structure derived from vigorous and unclear chemical/electrochemical reactions between Li metal and electrolytes. Since the 1970s, numerous efforts have been devoted to understanding the nature and characteristics of SEI on Li^0 (Li-SEI) using a variety of advanced characterization techniques, including X-Ray photoelectron spectroscopy (XPS),[10–13] Fourier transform infrared (FTIR),[10,14–16] nuclear magnetic resonance (NMR),[17,18] and cryogenic electron microscope (cryo-EM),[19–24] etc. So far, it has been widely acknowledged that the Li-SEI is composed of both inorganic and organic components with a complicated mosaic or multilayered structure,[6,19] and several key inorganic components (e.g., LiF and Li_2O, etc.) have been identified and quantified.[5,21,22,24]

[1]Hefei National Laboratory for Physical Science at Microscale, CAS Key Laboratory of Materials for Energy Conversion, Department of Materials Science and Engineering, University of Science and Technology of China, Hefei, Anhui 230026, China

[2]Department of Electrochemical Energy Storage, Helmholtz-Zentrum Berlin für Materialien und Energie, Hahn-Meitner-Platz 1, Berlin 14109, Germany

[3]Institute of Functional Nano and Soft Materials (FUNSOM), Soochow University, Suzhou, Jiangsu 215123, China

[4]School of Nano-Tech and Nano-Bionics, University of Science and Technology of China, Hefei, Anhui 230026, China

[5]i-LAB, CAS Center for Excellence in Nanoscience, Suzhou Institute of Nano-Tech and Nano-Bionics, Chinese Academy of Science, Suzhou, Jiangsu 215123, China

[6]CAS Key Laboratory of Soft Matter Chemistry, Department of Polymer Science and Engineering, University of Science and Technology of China, Hefei, Anhui 230026, China

[7]National Synchrotron Radiation Laboratory, University of Science and Technology of China, Hefei, Anhui 230029, China

[8]In situ Center for Physical Science, School of Chemistry and Chemical Engineering, Shanghai Jiaotong University, Shanghai 200240, China

[9]Materials and Process Simulation Center, Department of Chemistry, California Institute of Technology, Pasadena, CA 91125, USA

[10]Institute of Chemistry, University of Potsdam, 14476 Potsdam, Germany

[11]Battery Science Branch, Energy and Biomaterials Division, Sensor and Electron Devices Directorate, US Army Research Laboratory, Adelphi, MD 20783, USA

[12]These authors contributed equally

[13]Lead contact

*Correspondence:
yan.lu@helmholtz-berlin.de (Y.L.),
tcheng@suda.edu.cn (T.C.),
conrad.k.xu.civ@mail.mil (K.X.),
jiaosh@ustc.edu.cn (S.J.)

https://doi.org/10.1016/j.xcrp.2022.101057

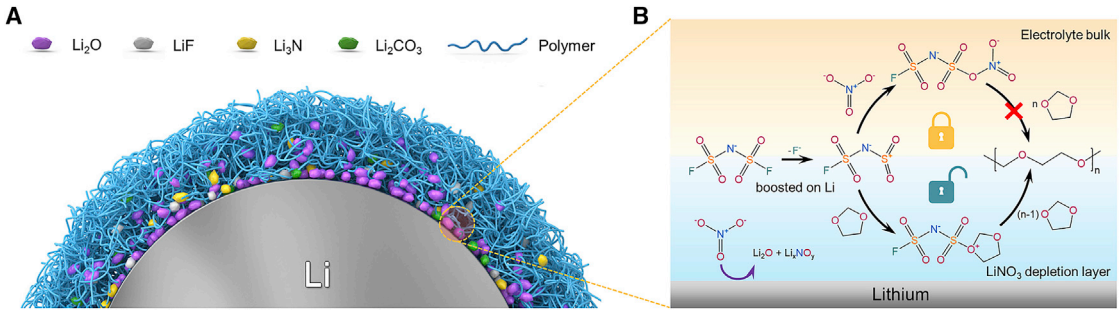

Figure 1. Interface-confined polymerization mechanism of the polymeric-inorganic SEI formation

(A) Schematic of the composition and structure of the SEI layer.

(B) The "locking and unlocking" polymerization mechanism of the SEI formation.

Despite the extensive investigations on the inorganic components in Li-SEI, the organic components have long been overlooked. As an important part of the Li-SEI, the organic components play essential roles in facilitating Li-ion transfer through SEI and regulating the mechanical properties of SEI to accommodate the drastic volumetric change of electrode during Li plating/stripping processes.[25] Over a long period, most of the organic components in the SEI are found to be low molecular-weight organic lithium salts and oligomers derived from the parasitic reactions between the electrolyte solvents and Li metal,[26,27] which are unable to provide enough flexibility to accommodate the volumetric change of Li metal anode. Therefore, the continuous rupture of the fragile pristine SEI and formation of new SEI has been unavoidable, which results in low CE of Li plating and stripping. Recently, long-chain organic polymers have been attempted to promote the reversibility of Li metal anode by improving the mechanical property and ionic conductivity of Li-SEI,[14,15,28–33] with extensive postmortem characterizations on the static state of Li-SEI at a specific charge/discharge state of batteries to understand the properties of SEI. However, the regulation of the organic-inorganic structure of Li-SEI remains a trial-and-error process rather than a rational design, mainly due to the poor understanding of the dynamic process of the ever-evolving Li-SEI, especially the formation mechanism of Li-SEI at a molecular level, and the evolution process of Li-SEI during the Li nucleation and growth.

Here we unveil a novel *operando* polymerization mechanism confined at the Li-electrolyte interface for the formation of a polymer-rich SEI in an electrolyte of lithium bis(fluorosulfonyl)imide (LiFSI) and $LiNO_3$ dissolved in 1,3-dioxolane (DOL) (denoted as LiFSI-$LiNO_3$-DOL). Comprehensive characterization techniques have been used to investigate the components and structure of the *operando* polymerized SEI. It reveals that the SEI is mainly composed of long-chain poly-DOL with an average molecular weight (avg. M_w) reaching up to 20,000 g mol^{-1} and inorganic components such as Li_2O, LiF, Li_3N, and Li_2CO_3 (Figure 1A), which renders the SEI with excellent flexibility and elasticity. The polymeric-inorganic composite SEI is formed through an interface-confined "locking and unlocking" polymerization process, which is initiated by the consumption of the polymerization inhibitor and locker $LiNO_3$ with the formation of inorganic Li salts at the electrochemical interface, followed by instantaneous polymerization of the cyclic ether solvent triggered by the initiator $FSO_2NSO_2\cdot$ radical (Figure 1B). The SEI exhibits excellent flexibility and elasticity properties during its evolution process, with a drastic self-thinning process through inflation and a further stretching process through a self-healing mechanism, which suppresses continuous SEI growth and enables an ultrahigh CE of 99.73% for Li plating and stripping (Figure S1 and Note S1).

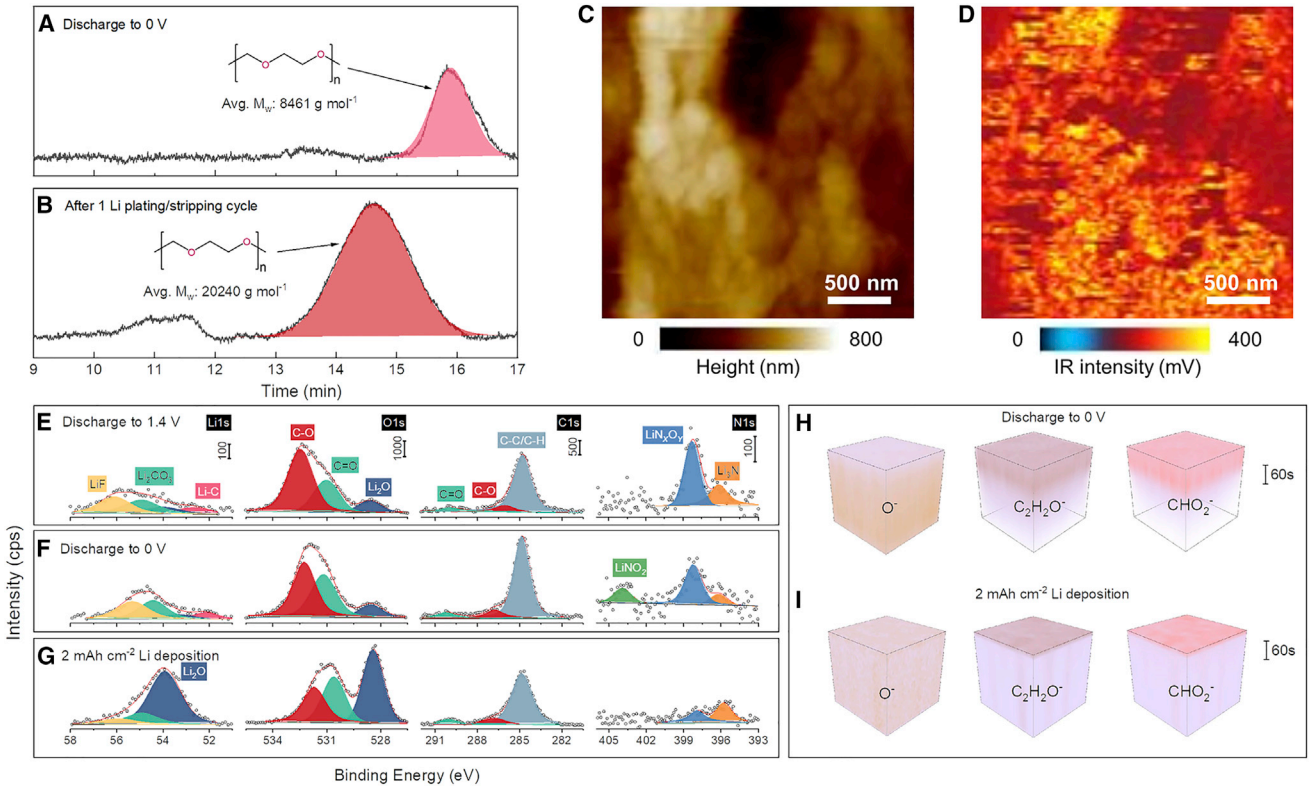

Figure 2. Characterization of the electrochemically formed SEI formed before the onset of Li nucleation and after Li deposition

(A and B) GPC results of the SEI formed upon discharge to 0 V at 0.1 mA cm^{-2} and after one Li plating-stripping cycle at 0.1 mA cm^{-2} for 0.5 mAh cm^{-2}.

(C and D) Topography (C) and the corresponding 2D mapping (D) of C-O stretches of the SEI based on AFM-nanoIR. The SEI layer was obtained on a Cu substrate in Li||Cu coin cell after one cycle of plating/stripping 3 mAh cm^{-2} Li at 0.5 mA cm^{-2}.

(E–G) XPS spectra of the SEI on Cu upon discharge to 1.4 V and 0 V and on 2 mAh cm^{-2} Li deposition obtained at 0.5 mA cm^{-2}.

(H and I) TOF-SIMS based 3D renders of O^-, $C_2H_2O^-$ and CHO_2^- upon discharge to 0 V and after Li deposition for 2 mAh cm^{-2} at 0.5 mA cm^{-2}. The x-y dimensions of the reneged volume are 100 × 100 μm.

RESULTS AND DISCUSSION

Chemical composition and structure of the polymeric-inorganic SEI

The presence of polymeric content in the SEI was identified by gel permeation chromatography (GPC) analysis of the SEI from discharged/cycled Li||Cu coin cells (Figures 2A, 2B, S2, and Table S1), which confirms the occurrence of polymerization process during the SEI formation. The avg. M_w of polymer in the SEI formed upon discharge to 0 V versus Li/Li$^+$ and prior to the onset of Li nucleation amounts to 8,461 g mol^{-1}, which increases to 20,240 g mol^{-1} after the first metallic Li plating-stripping cycle, indicating more intensive polymerization upon the presence of Li deposits. The polymeric compounds in the SEI layer were further identified to be poly-DOL, which, as the product from the familiar ring-opening polymerization of cyclic ethers and DOL here, is confirmed by atomic force microscopy-infrared nanospectroscopy (AFM-nanoIR) and synchrotron Fourier transform infrared (s-FTIR) spectra (Figures S3 and S4A). In those spectra, the peaks at 865 and 1,081 cm^{-1} are derived from the long-chain -CH_2- and C-O stretches of poly-DOL, respectively.[34] Two-dimensional mapping of C-O stretches in the SEI (Figures 2C, 2D, and S4B) reveals the homogeneous distribution of poly-DOL in the SEI layer.

To further elucidate the chemistry and structure of the polymeric-inorganic SEI, we performed depth-profiling XPS characterizations on the SEI formed on Cu

electrodes at various stages of the electrochemical process (Figures 2E–2G). The major content on the surface layer of the SEI formed upon discharge to 1.4 V versus Li/Li^+ is poly-DOL, according to the strong signals of C-C/C-H and C-O bonds in the C 1s and O 1s regions. Meanwhile, inorganic compounds, LiF, Li_2O, Li_3N, and Li_xNO_y, are also observed owing to the decomposition of the LiFSI and $LiNO_3$ in the electrolyte. When discharged to 0 V, no evident changes are observed in the spectra, suggesting that the chemical composition of the SEI surface remains rather stable. In comparison, the signals of Li_2O become significantly stronger when 2 mAh cm^{-2} Li is deposited. The XPS spectra after 30 s Ar sputtering (Figure S5) resemble those before sputtering, except that the signals related to poly-DOL become weaker, while the inorganic compounds, particularly Li_2O, appear more dominant. This indicates that the SEIs are rich in Li_2O in the inner part, while the outer layer is enriched with polymer.

To evaluate the three-dimensional distribution of polymeric and inorganic components in the SEI, time-of-flight secondary ion mass spectrometry (TOF-SIMS) experiments were carried out. In good agreement with the XPS results, TOF-SIMS also detects strong intensities of both inorganic compounds (indicator: O^-) and organic fragments arising from polymeric species (indicators: $C_2H_2O^-$ and CHO_2^-) (Figures 2H, 2I, S6A, and S6B), suggesting the existence of Li_2O adjacent to poly-DOL. Two-dimensional mapping of these fragments overlaps with each other (Figures S6C–S6J), indicating their homogeneous distribution at the micrometer scale, which is consistent with the s-FTIR-based mapping result (Figure S4B). Meanwhile, the uniform topography, together with the homogeneous distribution of the elastic modulus obtained from atomic force microscopy (AFM) (Figure S7), suggest that the polymeric-inorganic SEI layer is uniform in polymeric and inorganic compounds. These characteristics of the SEI ensure homogeneous Li-ion transport across the SEI.

In light of the spectral results, we unveil the chemical composition and structure of the polymeric-inorganic SEI formed by the "locking and unlocking" mechanism of polymerization. As illustrated in Figure 1A, both polymeric (poly-DOL) and inorganic (Li_2O, LiF, Li_3N, etc.) compounds are present and distributed evenly in the SEI, while gradients of inorganic and polymeric components still exist, with the former relatively concentrating in the inner and the latter enriched in the outer part of the SEI. The rich polymeric content promotes the flexibility of the polymeric-inorganic SEI, while the inorganic compounds, especially Li_2O, improve the compactness and mechanical strength of the SEI. Meanwhile, the homogeneous polymeric-inorganic distribution facilitates uniform Li-ion transport in the SEI, which suppresses the dendritic Li deposition contributing to high CEs.

Formation mechanism of the polymeric-inorganic SEI

To elucidate the forming process of the *operando* polymerized SEI, we conducted theoretical computations on the decomposition pathway of the LiFSI-$LiNO_3$-DOL electrolyte. The initial reductions of NO_3^- and FSI^- triggered by Li^0 were simulated using quantum mechanics-based molecular dynamics (QM-MD) (Figure 3A and Note S2). For FSI^-, we found that one of its S-F bonds easily splits into F^- plus one $FSO_2NSO_2\cdot$ radical (denoted as FSI-F) in the electrolyte, consistent with the previously reported FSI^- decomposition pathway.[35] Meanwhile, rapid and complete NO_3^- decomposition is observed in the QM-MD, which has received insufficient attention. These reactions start from the fast diffusion of NO_3^- to the Li anode, followed with quick breaking of all N-O and N=O bonds leading to the formation of Li_2O and Li_3N precipitates. Hybrid *ab initio* and reactive force field (HAIR) MD

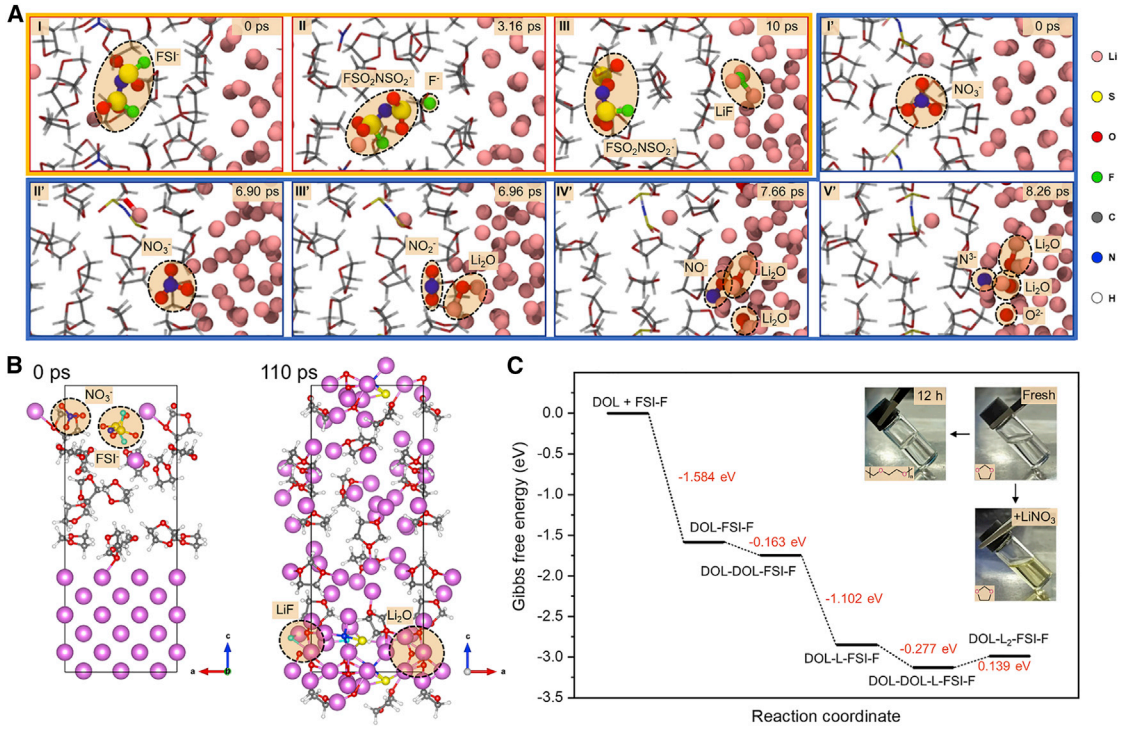

Figure 3. Theoretical computations on the SEI formation process

(A) The reactive snapshots of the decomposition of FSI^- (I-III) and NO_3^- (I'-V') based on QM-MD simulation of the LiFSI-$LiNO_3$-DOL system. The reactions involve (I, II) $FSI^- \rightarrow F^- + (\cdot)SO_2NSO_2F$, (I', II', III') $NO_3^- + 2e^- \rightarrow NO_2^- + O^{2-}$, (IV') $NO_2^- + 2e^- \rightarrow NO^- + O^{2-}$ and (V') $NO^- + 4e^- \rightarrow N^{3-} + O^{2-}$.

(B) The snapshots from HAIR-MD simulations of LiFSI-$LiNO_3$-DOL at 0 ps and 110 ps. Color code: H, white; Li, purple; C, gray; N, blue; O, red; F, cyan; S, yellow.

(C) Calculated Gibbs free energy profile of the ring-opening polymerization of DOL initiated by FSI-F radicals. The insets are photographs of as-prepared and aged electrolytes of 1 M LiFSI in DOL and the electrolyte with 4 wt.% $LiNO_3$ after 12 h aging.

simulations[36] were further used to investigate the decomposition processes of salts and solvent on Li^0 with an extended time scale (Figures 3B and S8–S11). The formation of FSI-F and the continuous reduction of NO_3^- are also captured using HAIR simulations (Figure S8). We also found that FSI-F subsequently decomposes via N-S bond cleavage to form LiF and Li_2O (Figure 3B). The DOL ring-opening process occurs after 110 ps, which further generates Li_2O, CO_2, C_2H_4, etc. (Figures S9 and S10). The significant decomposition of NO_3^- anions and DOL leads to the rich Li_2O content and high Li_2O/LiF ratio in the SEI layer (Figure S11). Meanwhile, the CO_2 generated may combine with O^{2-} from the decomposition of NO_3^- (Figure 3A), which may explain the presence of Li_2CO_3 in the XPS spectra (Figures 2E–2G).

Although the polymerization process (with a time scale far beyond the brute force atomic scale simulation) has yet been directly captured, density functional theory (DFT) calculations provide a detailed reaction pathway of DOL polymerization initiated by FSI-F radicals (Figures 3C and S12). It starts with the binding of a DOL molecule to the FSI-F radical forming a DOL-FSI-F complex, where the donation of the lone pair electrons from O of the DOL molecule to S of the FSI-F radical yields a strong binding energy of −1.584 eV from the DFT prediction. The formation of DOL-FSI-F complex activates the C-O bond in the DOL molecule allowing it to bind with another DOL molecule, which triggers a ring-opening reaction of the DOL molecule binding with the FSI-F radical, thus forming a DOL-L-FSI-F complex. The ring-opening reaction is energetically favorable with a Gibbs free energy (ΔG) of

−1.102 eV. The polymerization process propagates with a second DOL, whose binding with the DOL-L-FSI-F complex is also favorable, with a ΔG of −0.277 eV. ΔG of the following ring-opening reaction is slightly positive (0.139 eV) but surmountable at room temperature. Overall, the DFT predicted thermodynamics (Table S2) reveals that the FSI-F radical-initiated DOL polymerization is energetically favored.

The polymerization of DOL predicted by DFT calculations has been verified by the mixture of LiFSI and DOL, which forms a transparent liquid but polymerizes and solidifies spontaneously and uncontrolledly within 12 h forming a thick gel/polymer electrolyte (Figure 3C, inset and Figure S13A). This is probably caused by the defluorination of FSI^- anions in the presence of Li^+ in the electrolyte solution, forming FSI-F radicals that initiate the DOL polymerization. The defluorination of FSI^- can be facilitated by strong interactions between Li^+ (i.e., Lewis acid) and F^- (i.e., Lewis base) and the precipitation of LiF due to the virtual insolubility of LiF in organic solvents.[37] Notably, the DOL polymerization can be suppressed significantly by $LiNO_3$. With sufficient NO_3^- ($\geq$0.4 wt. %, Figure S14), the electrolyte remains as a fluid liquid (Figure 3B, inset, and Figure S13F). In addition, $LiNO_3$ can still prevent the continuous polymerization of the LiFSI-DOL solution, even after the polymerization reaction has been initiated (Figure S15). Therefore, NO_3^- serves as an effective inhibitor to the polymerization reaction in the electrolyte solution. The underlying mechanism is that NO_3^- binds stronger to FSI-F radicals than the DOL molecule (−3.911 eV versus −1.584 eV, Table S3), which drastically suppresses the formation of the DOL-FSI-F complex. Meanwhile, $LiNO_3$ also boosts the reduction stability of FSI-F radical (Figure S16).

Based on the results above, we propose a controlled "locking and unlocking" mechanism of the interphase-confined *operando* polymerization for the formation of polymeric-inorganic SEI in the LiFSI-$LiNO_3$-DOL electrolyte, as illustrated in Figure 1B. (1) The "unlocking" polymerization at the Li-electrolyte interface is because of the consumption of polymerization inhibitor $LiNO_3$. Spontaneous defluorination of FSI^- takes place on the aggressively reductive Li^0 (or on Cu at low voltage versus Li/Li^+), which derives FSI-F radicals as an initiator for DOL polymerization. In the meantime, the polymerization inhibitor $LiNO_3$ decomposes at the Li metal-electrolyte interface forming inorganic Li salts (e.g., Li_2O and LiN_xO_y), which largely contribute to the inner part of the SEI, resulting in a temporary $LiNO_3$-depletion layer near the Li metal surface. The emergence of this temporary $LiNO_3$-depletion layer promotes the interaction of FSI-F radicals with DOL molecules, instantaneously inducing the ring-opening polymerization of DOL at the Li-electrolyte interface to form the outer part of the SEI. This polymerization process terminates after a layer of uniform and stable SEI is formed on the surface of Li^0 due to the weaker electrical activation of FSI-F. Besides, the polymerization is "unlocking" after the decomposition of $LiNO_3$ forming inorganic Li salts like Li_2O, which explains the phenomenon that the inner part of the SEI is rich in Li_2O while the outer part contains more polymer. (2) The "locking" DOL polymerization in the electrolyte bulk results from the co-existence of polymerization initiator and inhibitor. A high concentration of $LiNO_3$ interacts with the FSI-F radicals in the bulk electrolyte, which effectively blocks interactions of the FSI-F radicals with DOL molecules and prevents the bulk electrolyte from polymerization. Therefore, the radical-induced polymerization is localized at the Li-electrolyte interface, which completely differs from the cation-initiated and continuous DOL polymerization that results in polymerized or gelled electrolyte with relatively poor Li-ion diffusion kinetics.[30,32]

The controlled polymerization mechanism can be extended beyond the DOL-FSI-F complex and to alternative anions (Figures S16 and S17). Table S4 shows ΔG of

different anions binding to the FSI-F radical, which can be used to evaluate their ability to prevent DOL polymerization. When the ΔG is more negative than that of the binding between the FSI-F radical and DOL molecule (−1.584 eV, −36.52 kcal mol^{-1}), DOL polymerization would be suppressed or inhibited, and otherwise not. Our results reveal that ClO_4^- cannot effectively suppress the DOL polymerization since the ΔG for FSI-F radical reacting with ClO_4^- is −1.53 eV (−36.52 kcal mol^{-1}), comparable to that between the FSI-F radical and DOL molecule. In comparison, the ΔG of NO_2^- interacting with the FSI-F radical is much more negative (−2.718 eV = −62.68 kcal mol^{-1}), suggesting that NO_2^- is capable of inhibiting the DOL polymerization. These calculation predictions have been verified experimentally, where the LiFSI-$NaNO_2$-DOL electrolyte preserves the liquid state over a month (Figure S13D), while the LiFSI-$LiClO_4$-DOL electrolyte solidifies within 2 days (Figure S13B).

Morphological evolution of the polymeric-inorganic SEI under Cryo-TEM and *in situ* EC-AFM

We further performed cryogenic transmission electron microscopy (cryo-TEM) characterizations to investigate the morphological evolution of the polymeric-inorganic SEI layer during an Li plating process. Figure 4A shows that thick (~100 nm) and wrinkled SEI layers are formed at the initial stage of Li deposition (150 s). Surprisingly, the SEI gets drastically stretched and thinned to ~20 nm after 12 min Li deposition and eventually to 7 nm after 24 min Li deposition (Figures 4B and 4C), which suggests the polymerized SEI is highly flexible and compact and agrees well with its polymer-rich feature. The organic/polymeric nature of the SEI layer is also corroborated by the extremely high sensitivity of the SEI to the electron beam during cryo-TEM imaging (Figures S18–S23, Videos S1, S2, S3, S4, S5, and S6, and Note S3).

The polymer in the SEI endows it with excellent flexibility to thin down and accommodate the large volumetric expansion of Li during the Li growth. Meanwhile, the inorganic Li salts endow the SEI with the high compactness to prevent the severe penetration of electrolytes after the stretching, which inhibits the decomposition of electrolytes and further growth/re-thickening of the SEI. Such a high compactness and excellent flexibility minimizes the breaking/repairing and continuous growth of the SEI, which mitigates the active Li loss and contributes to the ultrahigh CEs. Therefore, the compactness and flexibility are two important parameters for the SEI, which requires the sophisticated mixing and appropriate ratio of the polymeric and inorganic compounds in the SEI. The apparent thinning of the SEI in microscope agrees with the rendered 3D illustrations of O^-, $C_2H_2O^-$, and CHO_2^- fragments in Figures 2H and 2I, which shows that the SEI on the Li deposits appears to be significantly thinner than that formed on discharge to 0 V and before Li nucleation.

The *ex situ* morphologies of these Li deposits were revealed by micrographs and tomograms based on cryo-TEM and SEM (Figures 4D–4F, S24–S26, and Videos S7, S8, and S9). Li deposits of 150 s appear like deflated balls (the deflation might be a consequence of galvanic corrosion[17]) with its walls made of the SEI layer (Figures 4D and S24A). In the following process, the morphology of Li deposits progresses gradually from partially to fully filled balls and then to a bar shape. The balls range from 100 nm to 1 to 2 μm, while the bars are 2 to 4 μm in diameter and several to tens of micrometers in length (Figure S25). Tomography images and videos (Figures S24B and S24C, and Videos S7, S8, and S9) show that these large balls (Figure S24B) and bars (Figure S24C) are plump without evident cracks or pits. With the proceeding of deposition, the Li bars grow longer and bend, eventually leading to a flat surface (Figure S25F) due to mechanical compression from the stack pressure

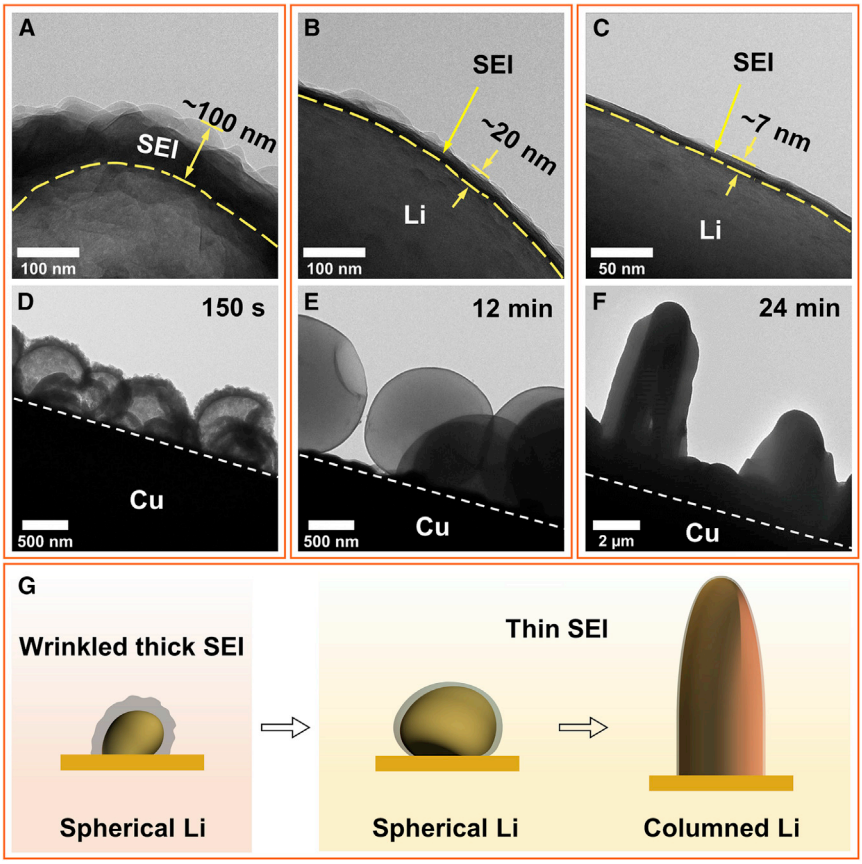

Figure 4. Morphological evolution of Li deposition and the interface-confined SEI

(A–C) Cryo-TEM images of the SEI layers on 150 s (~0.02 mAh cm^{-2}), 12 min (0.1 mAh cm^{-2}), and 24 min (0.2 mAh cm^{-2}) Li deposits.

(D–F) Cryo-TEM micrographs. The total electron dosage used for imaging amounts to 15, 20.5, 41, 2.5, 0.75, and 0.25 e $Å^{-2}$ for (A), (B), (C), (D), (E), and (F), respectively.

(G) Schematic of the morphological evolution of Li deposition and SEI.

inside the coin cells. These micron-sized Li deposits, either spherical or bar-like, exhibit low tortuosity and high surface smoothness, which contributes to negligible "dead" Li^0 upon Li stripping and high CEs for Li plating/stripping.[38]

Figure 4G schematically illustrates the process of SEI formation and Li^0 growth. The SEI formation happens mainly at the initial stage of Li deposition (Figure S27 and Table S5), forming thick and wrinkled polymeric SEI shells. Subsequently, Li ions travel across the ionically conductive SEI and get reduced underneath as the deposition proceeds, gradually inflating the SEI, and stretching and thinning the SEI shells. The Li^0 deposits appear like an inflated ball with a smooth surface, probably due to the uniformity of the SEI shell that induces the homogeneous Li-ion transport and conformal growth of Li deposits. Subsequently, Li^0 balls grow toward Li^0 bars, and the SEI gets further stretched along the direction perpendicular to the electrode/electrolyte interface, whose polymeric shell effectively constrains the volumetric expansion of Li deposition through its own flexible deformation.

In situ electrochemical AFM (EC-AFM) was performed to investigate the real-time nucleation and growth of Li^0 that simulates the condition of real batteries (Figure 5A, S28, S29, and Video S10). AFM images in Figure 5 show the morphological evolution

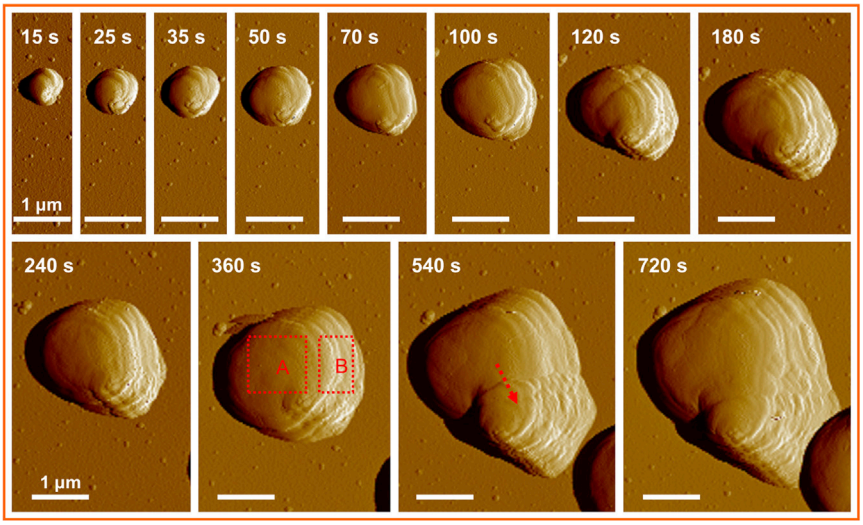

Figure 5. Morphological evolution of Li deposits monitored by *in situ* EC-AFM

Li deposition was obtained on a Cu substrate at 0.5 mA cm^{-2} for 720 s. All scale bars, 1 μm. Regions A and B indicate the different deposition morphologies between the top and sides of the deposited Li. The red arrow represents the growth direction of deposited Li.

of a single Li^0 particle formed during electrodeposition. Unlike the concave morphology of the initial Li deposition revealed by *ex situ* probes (including AFM in Figure S30, SEM in Figures S25A–S25C, and cryo-TEM in Figures 4D and 4E and S24A), the deposited Li^0 appears to be plump spheres (Figures S28A–S28J) under *in situ* AFM, due to the absence of galvanic corrosion. The Li^0 deposits after 540 s are obviously elongated in the region as marked by red arrows in Figure 5. The size of deposited Li gradually grows from 600 nm at the initial 15 s to 3 μm at 720 s, which is equivalent to a volumetric expansion rate of more than 100 times.

Nanoscale morphological differences of Li surface can also be identified by the surface micrographs in Figure 5. The top of the deposited Li (Region A) is smooth and flat, while peculiar texture patterns are clearly visible on the side of the Li^0 particles (Region B), which are also verified by the *ex situ* SEM image (marked by red arrows in Figure S25D) and Cryo-TEM based 3D tomograms (Figure S24). These wrinkled patterns are similar to stretched marks left on the skin due to the rapid growth of the human body, suggesting the self-thinning and self-healing process of the polymeric-inorganic SEI at the fast-growing areas of Li deposition. The polymerized SEI drastically stretches itself during the initial Li growth, and consequently repairs itself instantaneously at overstretched regions thanks to the fast *operando* polymerization of DOL confined at the Li-electrolyte interface.

The *operando* polymerized Li-SEI demonstrates significant advantages to promote the reversibility of Li metal anodes: (1) It exhibits excellent mechanical flexibility and self-healing property upon breakage and exposure of freshly deposited Li to the liquid electrolyte during cycling, which effectively prevents exposure of new Li^0 surfaces, and suppresses the localized Li deposition and continuous SEI growth. (2) It facilitates fast and homogeneous Li-ion conduction due to the nanometer thickness and homogeneity of the polymerized interphase. Therefore, the *operando* polymerized Li-SEI promotes spherical or bar-like Li deposits with low tortuosity and low surface areas, contributing to negligible "dead" Li^0 evolution upon Li stripping and minimizing the consumption of Li to form the SEI for an ultrahigh CE of 99.73% for

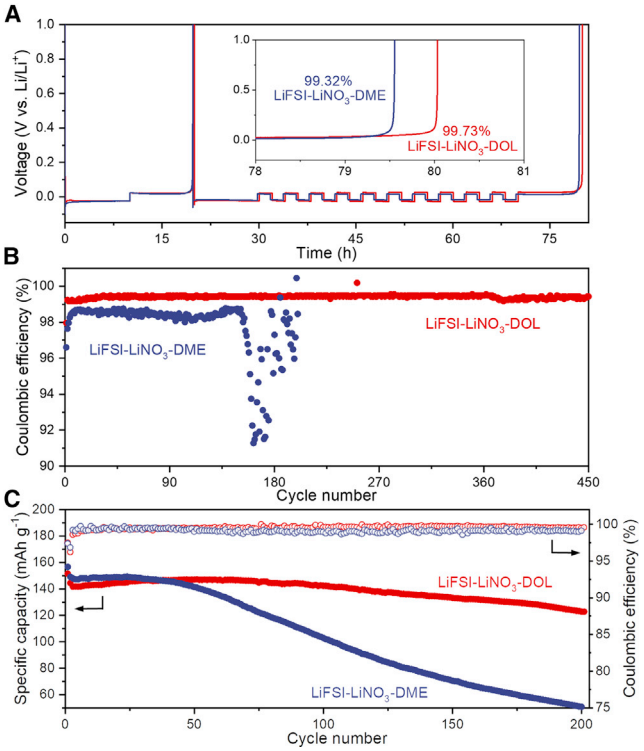

Figure 6. Electrochemical performance of Li metal batteries in LiFSI-$LiNO_3$-DOL and LiFSI-$LiNO_3$-DME electrolytes

(A) Voltage-time profile of Li plating/stripping based on the method by Zhang et al.[39]

(B) Coulombic efficiency of Li plating/stripping at a current density of 0.5 mA cm^{-2} and plating capacity of 2 mAh cm^{-2} for each cycle.

(C) Specific discharge capacity and Coulombic efficiency of Li||LFP full cells (N/P ratio = 1) cycled at 0.33C between 2.6 and 3.8 V (1 C = 160 mAh g^{-1}).

metallic Li plating/stripping (Figure 6A). In comparison, a lower CE of 99.32% is obtained in the 1,2-Dimethoxyethane (DME)-replacing electrolyte (LiFSI-$LiNO_3$-DME) without such an *operando* polymerization process. Moreover, the *operando* polymerized SEI enables better electrochemical kinetics (Note S4) and facilitates better long-term cycling stability in Li/Cu half cells (Figure 6B) and Li||LFP full cells (Figure 6C) with a low N/P ratio of 1 (N/P ratio is defined as the capacity of negative electrode to capacity of positive electrode).

Based on the above chemical/electrochemical and morphological analyses, we conclude that (1) fast and homogeneous Li-ion transport and (2) high flexibility and compactness are the two most important key performance indicators (KPIs) of an ideal Li-SEI. (1) To satisfy the first KPI, homogeneous distribution of inorganic Li-salt (e.g., LiF and Li_2O) grains within an interconnected polymeric framework (high polymerization degree) in the SEI layer and the intimate interfacial contacts between each other would be essential to accelerate Li-ion diffusion throughout the polymeric network. A low SEI thickness is also crucial to reduce the Li-ion diffusion distance. (2) The second KPI requires an optimal polymeric/inorganic ratio in the SEI layer. An inorganic-organic composite with the inorganic content too high suffers from the sluggish Li^+ conduction and increasing brittleness, which is more prone to cracking, once it is enriched with inorganic Li salts. For comparison, when organic/polymeric content is dominant, the SEI struggles with the poor capability of preventing the electrolyte penetration of electrolytes and continuous SEI growth.

In this work, we unveil the formation process of an *operando* polymerized SEI through the "locking and unlocking" mechanism of interface-confined polymerization in a cyclic ether-based electrolyte, which can only be "unlocking" by Li^0 at the electrochemical interface while being "locking" in the electrolyte bulk. Our study further reveals that the FSI-F radical acts as an initiator, while $LiNO_3$ as an inhibitor, for the polymerization of DOL. This *operando* formed SEI is a conformal polymeric-inorganic composite that exhibits fast and homogeneous transport of Li ions, facilitating micron-sized and low-tortuosity Li deposition. With the excellent flexibility and robustness, the polymeric-inorganic SEI effectively accommodates Li^0-growth by 100 times through stretching and healing itself while still preventing the newly deposited Li from exposure to the liquid electrolyte. In this way, irreversible capacity loss is minimized with this thin and flexible SEI, leading to an ultrahigh Li plating-stripping CE of 99.73%. This "locking and unlocking" mechanism of the polymeric-inorganic SEI formation sheds light on the elusive dynamic process of SEI, guiding us to establish the KPIs of an ideal Li-SEI and to develop the rational design of SEI for practical Li metal batteries.

EXPERIMENTAL PROCEDURES

Resource availability

Lead contact

Further information and requests for the resources are available from the lead contact, Shuhong Jiao (jiaosh@ustc.edu.cn).

Materials availability

No unique materials were generated by this study.

Data and code availability

The data that support the findings of this study are available from the corresponding authors on reasonable request.

Materials

Battery-grade LiFSI (99.8%), $LiNO_3$, and DME (99.95%) were purchased from DoDo Chem, and DOL (99.8%, anhydrous) from Sigma-Aldrich. LiFSI and $LiNO_3$ were dried at 80°C for 12 h before use. DOL and DME were used as received. Molecular sieves were dried at 500°C for 3 h and transferred immediately to the transfer chamber of the glove box before use. $LiFePO_4$ (LFP) cathode material was kindly provided by Yuhuang Co. Carbon-coated Al foil (purity) was purchased from Alfa Asear. Li foils (250-μm thick, 1.91-cm diameter) and copper (Cu) foil (25 μm in thickness) were purchased from KeJing MTI Corporation. Li was used as received, while the Cu foil was washed with ethanol (1×), 1 mol L^{-1} hydrochloric acid (99%, SCRC) (1×), ethanol (1×) and acetone (purity, SCRC) (1×). The Cu foil was dried in a vacuum drying oven, and then transferred to the glovebox. All of the chemicals except ethanol, hydrochloric acid, and acetone were kept and handled in a glovebox (Mikrouna) circulated with high-purity argon gas (<1 ppm O_2 and <1 ppm H_2O). The working electrolyte was 1 M LiFSI in DOL with 4 wt.% $LiNO_3$. Meanwhile, 1 M LiFSI-DME + 4 wt.% $LiNO_3$ and commercial 1M $LiPF_6$ in EC/DMC (v/v = 1:1) were tested as reference electrolytes. Note that 4 wt.% $LiNO_3$ is close to the saturation concentration in 1 M LiFSI-DOL. The poly-DOL were obtained from 1 M LiFSI-DOL (without $LiNO_3$ additive) after 48 h aging for full polymerization. The characterization of LiFSI-$LiNO_3$-DOL electrolyte and poly-DOL is shown in Note S5.

Electrochemical testing

All of the electrochemical tests were performed using CR2032 coin-type cells placed in a temperature-constant chamber operating at 25°C. In each cell, a piece of Celgard 2,325 separator and 40 μL electrolyte were used.

Li||Li symmetric cells and Li||Cu half cells

In Li||Li symmetric cells, two pieces of Li chips (250 μm in thickness) were used as the working and the counter electrode. In Li||Cu half cells, a Li chip (250 μm in thickness) was used as the reference and the counter electrode and a piece of Cu foil was used as the working electrode. Cyclic voltammetry tests in the range between 1 and −0.4 V versus Li/Li^+ were performed using Li||Cu cells with a piece of Li foil as the reference and the counter electrode and a piece of Cu foil as the working electrode by using CHI760E electrochemical workstation (CH Instruments), at a scanning rate of 5 mV s^{-1}. Electrochemical impedance spectroscopy (EIS) in the frequency of 100 kHz to 0.1 Hz (amplitude: 10 mV) was performed using Li||Cu cells, measured by Solartron analytical EnergyLab. Before the EIS test, the cells were performed a linear sweep voltammetry process from 1 to −0.4 V versus Li/Li^+, at a scanning rate of 5 mV s^{-1}.

Li||$LiFePO_4$ (LFP) full cells

Li||LFP full cells were constructed by using a piece of copper foil with 100% excess Li or a piece of Li chip as the anode, a piece of LFP electrode (1.13 cm^2) as the cathode, and a piece of 2,325 separator. LFP cathode preparation: The LFP electrode was prepared by casting the slurry mixture (80 wt.% active material, 10 wt.% TIMCAL Graphite & Carbon Super P (KeJing MTI Co) and 10 wt.% HSV900 poly(vinylene fluoride) binder (KeJing MTI Co) in N-methyl-2-pyrrolidone) onto the carbon-coated aluminium (Al) current collector foil via blade-coating. The active material mass was ∼9.4 mg (∼8.3 mg cm^{-2}). The LFP cathode was dried at 110°C overnight to remove the moisture. The dried LFP electrode was immediately transferred to the glovebox to prevent degradation.

Characterization

All electrode samples for characterizations were obtained from cycled Li||Cu coin cells. Cells were dissembled in the glovebox before the characterizations. All of the samples except GPC samples were rinsed with DOL to remove the electrolytes left on the surface of the electrodes and dried in the glove box.

SEM

Morphological characterizations of the plated Li on the Cu working electrodes (applying a negative polarization for different times on the Cu electrodes at a current density of 0.5 mA cm^{-2}) were performed by scanning electron microscopy (SEM; FEI Apero), where the Helios accelerating focused ion beam was set as 2 kV. The electrode samples were sealed in an airtight container during transfer. Once the container was opened, the samples were loaded into the vacuum chamber of SEM within 10s.

Cryo-TEM

Eppendorf tubes containing the TEM grids (bare Cu TEM grids, 600 Mesh, Science Services, Munich, Germany) with Li deposits were immersed into a Dewar filled with liquid nitrogen (LN_2) and were then crushed quickly with a cutter plier while immersed in LN_2 in order to avoid exposing the TEM grids to the ambient atmosphere. The TEM grids were either transferred directly to a JEOL JEM-2100 transmission electron microscope (JEOL GmbH, Eching, Germany) using a cryo transfer tomography holder (Gatan 914; Gatan, Munich, Germany) or stored in LN_2. Imaging was carried out at temperatures around 90 K and the TEM was operated at an acceleration voltage of 200 kV. Cryo-TEM micrographs were recorded at several magnifications with a bottom-mounted 4k × 4k CMOS camera (TemCam-F416; TVIPS, Gauting, Germany). Tomographic tilt series were acquired using the Serial-EM acquisition software package[40] with a tilt range of ±60° and a 2° angular increment.

Tilt series were aligned using patch tracking and then reconstructed using weighted back-projection with the IMOD software package.[41] Segmentation was performed using Amira (FEI Company, Eindhoven, The Netherlands) and movies of segmented volumes were generated with UCSF Chimera.[42]

GPC

The molecular weight distributions of the polymer in SEI or electrolytes were performed by GPC (Elite P230II) equipped with a refractive index detector (Shodex R1-201H) and an Agress O1100 column oven with the eluent (THF, 40°C) at 1.0 mL min^{-1} 5 mg poly-DOL dissolved in 2 mL THF (Sigma-Aldrich), and the polymer composition of the SEI on Cu surface (washed by DME) dissolved and enriched by THF solvent for GPC analysis. GPC analysis of the SEI formed upon discharge to 0 V was prepared from the cells discharged to 0 V at 0.1 mA cm^{-2} then held at 0 V for 8 h, and the cycled one was obtained from the cells after one Li plating-stripping cycle at 0.1 mA cm^{-2} for 0.5 mAh cm^{-2}. Two hundred microliters of as-prepared electrolyte was dispersed in 2 mL THF before concentration, and the cycled electrolyte was obtained from the separators extracted from the cycled coin cells. In order to collect enough polymer, at least 20 coin cells were required in each extraction experiment for GPC testing. All the enrichment processes are implemented by the evaporation of excess THF to 200 μL at room temperature.

Synchrotron FTIR

The synchrotron FTIR spectra and imaging of the Cu electrodes (with SEI on top) after three Li plating-stripping cycles in Li||Cu coin cells (at 0.5 mA cm^{-2} for 1 mAh cm^{-2}) were collected on the infrared spectroscopy and microspectroscopy beamline (BL01B) at the National Synchrotron Radiation Laboratory (NSRL), China, which is equipped with a Bruker Vertex 70 FTIR spectrometer coupling with a Hyperion 2000 microscope. The spectra were measured in the range of 3,900 to 600 cm^{-1} with a total of 32 scans at aperture of 6 × 6 μm, coupled with mapping step size 25 μm. All of the spectra were smoothed three times and normalized with the Bruker OPUS software. The data were used to determine the distribution of polymer compounds on the cycled Cu electrodes.

The cycled Cu electrodes were transferred in an airtight container. Before the tests, all of the samples were exposed in the air for an hour to allow the Li alkoxides in the SEI to be converted to carbonates by reacting with CO_2 and H_2O in the air, which usually completes within few minutes at room temperature.[43] Polymer compounds like polyethers in the SEI are stable in the air,[26] and thus remained after air exposure. Therefore, the remaining C-O species detected by FTIR would be related to the polymer compounds.

AFM-nanoIR

Topography and chemistry of the SEI layer were studied by a nanoIR3 system (Bruker) equipped with Bruker Hyperspectral QCL. The SEI sample was obtained by plating Li on the Cu electrode (areal capacity of 3 mAh cm^{-2}) in the Li||Cu coin cell with a current density of 0.5 mA cm^{-2}, and then completely stripping the plated Li with a cutoff voltage of 1 V versus Li/Li^+. Both topography and AFM-IR measurements were conducted in the contact mode. The IR spectrum in the range of 800 to 1,900 cm^{-1} was recorded with the spectral resolution of 2 cm^{-1}.

AFM

The topography of the plated Li (areal capacity: 1 mAh cm^{-2}) was obtained with AFM (Dimension Icon, BRUKER) in the peak force tapping mode with sharp AFM tips (Bruker ScanAsyst Air). The modulus distribution of the SEI layer above the Li was

obtained in peak force quantitative nanomechanical mapping (QNM) mode with sharp AFM tips (Bruker RTESPA-300). After the electrochemical processes, the cells were dissembled in the glovebox and the samples were rinsed with DOL. Then the samples were loaded onto the sample stage of AFM, which was placed in the same glovebox, thus preventing the exposure of samples in the air. For the peak force QNM mode, the indentation depth was set at 5 nm. Since the thickness of the SEI layer is generally >10 nm and >7 nm in this work, the modulus was from the SEI layer rather than Li metal.

In situ *EC-AFM*

The Cu film prepared by the magnetron sputtering system (JGP450, SKY Technology Development Co., Ltd., CAS) was used as a flat substrate (working electrode) for Li deposition. Cu was deposited on the mica flakes with atomic level flat surface for 30 min, and the sputtering pressure and power were 0.4 Pa and 50 W, respectively. All *in situ* AFM height images and corresponding peak-force error images were obtained in the peak force tapping mode on Dimension Icon AFM (BRUKER, in the glovebox) with sharp AFM tips (Bruker ScanAsyst Fluid). The electrolyte of 1 M LiFSI in DOL with 4 wt.% $LiNO_3$ was used as the working electrolyte. A piece of Li ring was used as the reference and the counter electrode. The schematic diagram of *in situ* AFM is shown in Figure S31, and the *in situ* EC-AFM fluid cell was obtained from Bruker Corporation. CHI760E electrochemical workstation was used for galvanostatic tests at a current density of 0.5 mA cm^{-2}. The electrochemical cell was held at 0 V when acquiring AFM images. During the whole test, the electrochemical cell was relatively sealed to prevent the volatilization of the electrolyte.

XPS

SEI chemistry for Cu electrodes at different discharge state (discharging Li||Cu coin cell to 1.4 V and 0 V versus Li/Li^+, or passing through areal capacity of 2 mAh cm^{-2} on Cu electrodes) were performed by XPS (PHI-5000 VersaProbe) with a focused monochromatic Al Kα X-ray source. All the spectra results were calibrated with the C 1s photoemission peak at 284.8 eV to get rid of the charging effect. Depth-profiling results were obtained after Ar cluster ions sputtering (5 keV) on samples for 30s. All samples from the glove box were transferred to an airtight container to avoid air exposure. All of spectra were fitted using the XPSpeak software.

TOF-SIMS

SEI chemistry depth profiles for Cu electrodes discharged to 0 V and for 4 h (areal capacity of 2 mAh cm^{-2}) were obtained by a time-of-flight secondary ion mass spectrometer (TOF.SIMS5-100) with a 1 keV Cs^+ beam for sputtering. A 10 keV Bi^+ beam was used for analysis over a 100 μm × 100 μm area.

NMR

1 M LiFSI/DOL with 4 wt.% $LiNO_3$ (200 μL) or solid poly-DOL (30 mg) were dispersed in 0.5 mL DMSO-d_6 (Sigma-Aldrich) using an airtight NMR tube for ^1H and ^{13}C NMR experiment, which was recorded on a Bruker AVANCE III 400 spectrometer. ^1H and ^{13}C spectra were referenced to DMSO-d_6 at 2.50 ppm (δ ^1H) and 39.5 ppm (δ ^{13}C).

Computational details

In the QM-MD simulation, we used 1 LiFSI - 1 $LiNO_3$ - 14 DOL to simulate the LiFSI-$LiNO_3$-DOL electrolyte. The Li anode was simulated by using 3 by 3 by 6 Li (100) surface with 54 Li atoms. The vacuum between the anode and its periodic image is set according to the experimental density of the three electrolytes, respectively. Then, the components of the electrolyte were randomly inserted to the vacuum, forming

the electrolyte/anode half-cell with two explicit electrolyte/anode interfaces. We then carried out QM optimization followed by MD equilibration and 10 ps MD NVT simulation to investigate the initial reaction. Significant initial chemical reactions were observed in 10 ps of QM-MD simulations for these three systems. The QM-MD calculations were carried out using the VASP software[44,45] (version 5.4.4).

In the hybrid *ab initio* and reactive force field reactive dynamics-molecular dynamics (HAIR-MD) simulations, the Li metal anode was represented by a six-layer (3 × 3) supercell slab. Where the two bottom layers of the slab were fixed, we used the Li (100) surface to react with the electrolyte. To represent the electrolyte, we placed 13 DOL molecules in a periodic box. The desired 1 M concentration of Li salts is achieved with one molecule of LiFSI and $LiNO_3$ and the final simulation periodic cell was 10.5 × 10.5 × 26.5 Å, approximately. During the HAIR-MD simulation procedure, molecular dynamics simulations start with the AIMD (0.5 ps), followed by ReaxFF MD (5 ps), and continued alternatively using the NVT ensemble at 300 K, which lasts for 550 ps (100 cycles) with a 10-time acceleration. The timesteps for AIMD and ReaxFF were set at 1 fs and 0.25 fs, respectively, to guarantee good energy conservation during the HAIR simulations while ensuring efficient convergence for collisions and smooth reactions. The AIMD simulations are carried out using the Vienna *ab Initio* Simulation Package (VASP 5.4.4) while the ReaxFF simulations used the Large-scale Atomic/Molecular Massively Parallel Simulator (LAMMPS 2018) software.

Although it is almost impossible to directly capture the polymerization due to its limited time scale, the most favorable reaction pathway (Figure S12) has been proposed based on our previous study[46] and confirmed from hybrid function calculations. To study the mechanism of DOL molecular polymerization, molecular geometries of all model were optimized without constraints by DFT calculations using the B3LYP functional[47] with 6-31G(d) basis set for all atoms. To take the dispersion interactions into account, we consider the DFT-D3 dispersion correction.[48] The vibrational frequencies were computed at the same level to evaluate its zero-point vibrational energy and thermal corrections at 298 K. In terms of considering solvent effects, the single-point energy calculations were performed at the B3LYP with the 6-311+G(d,p) basis set level for all atoms. Besides, solvent effects were considered using the continuum solvent model SMD[49] for 1,3-dioxolane (DOL, dielectric constant is 7.13), which was used as the solvent in this experimental study. The Gibbs free energy for each species is taken as the sum of the thermal correction to free energies in the gas phase and the single-point energy in solution.

The time-dependent density functional theory (TD-DFT)[50,51] was used to explore the electronic properties of different acidic group with FSI-F systems. The frontier molecular orbitals (FMOs) and their energies were obtained at B3LYP/6-311+G(d,p) level. At the same time, the solvent effects of DOL were considered by using the continuum solvent model SMD. All calculations were performed with the Gaussian 16 suite of programs[52] (Revision A.01).

SUPPLEMENTAL INFORMATION

Supplemental information can be found online at https://doi.org/10.1016/j.xcrp.2022.101057.

ACKNOWLEDGMENTS

S.J. and R.C. acknowledge support by the National Key Research and Development Program of China under Grant No. 2017YFA0206700, the National Natural Science

Foundation of China (Grant Nos. 52072358 and 51902304), the Anhui Provincial Natural Science Foundation (Grant No. 1908085ME122), and the Fundamental Research Funds for the Central Universities (Grant No. Wk2060140026). The authors thank H. Sun, F. Peng, and Y. Liu from Bruker for the help with *in situ* AFM and Nano-IR experiments. We thank Infrared Spectroscopy and Micro-spectroscopy Station (BL01B) of National Synchrotron Radiation Laboratory (Hefei, China) for synchrotron FTIR experiments. We appreciate Vacuum Interconnected Nanotech Workstation (Nano-X), Suzhou Institute of Nano-Tech and Nano-Bionics, and the Chinese Academy of Sciences (Suzhou, China) for TOF-SIMS and XPS tests. Y.X. acknowledges financial support from the Alexander von Humboldt Foundation for a Humboldt Fellowship for Postdoctoral Researchers. Y. Lu thanks the Joint Lab for Structural Research at the Integrative Research Institute for the Sciences (IRIS Adlershof).

AUTHOR CONTRIBUTIONS

S.J. designed the project and conceptualized the idea. S.J., R.C., Y.Lu, Y.J., Y.X., and Y.C. conceived the experiments. Y.J., Y.C., and X.L. performed the electrochemical/chemical measurements and analyzed the data. Y.X. and Z.K. conducted the cryo-TEM observation and data analysis under the supervision of Y.Lu and M.X., and Y.Liu performed MD or HAIR simulations and DFT calculations under the supervision of T.C. and W.G. Y.C. and F.H. conducted the *in situ* EC-AFM experiments and data analysis. Y.C. and P.S. performed GPC tests under the supervision of Y.Y., Z.L., and S.W., and Y.C. performed SEM tests. L.Z. conducted XPS and TOF-SIMS experiments and data analysis under the supervision of Y.S. and L.C. Y.X., Y.J., Y.C., M.X., R.C., X.R., K.X., T.C., W.G., and S.J. participated in the discussion and wrote the manuscript, and all authors were involved in revising the manuscript.

DECLARATION OF INTERESTS

The authors declare no competing interests.

Received: April 13, 2022
Revised: July 8, 2022
Accepted: August 30, 2022
Published: September 27, 2022

REFERENCES

1. Liu, J., Bao, Z., Cui, Y., Dufek, E.J., Goodenough, J.B., Khalifah, P., Li, Q., Liaw, B.Y., Liu, P., Manthiram, A., et al. (2019). Pathways for practical high-energy long-cycling lithium metal batteries. Nat. Energy *4*, 180–186. https://doi.org/10.1038/s41560-019-0338-x.

2. Lin, D., Liu, Y., and Cui, Y. (2017). Reviving the lithium metal anode for high-energy batteries. Nat. Nanotechnol. *12*, 194–206. https://doi.org/10.1038/nnano.2017.16.

3. Zhang, J.-G., Xu, W., Xiao, J., Cao, X., and Liu, J. (2020). Lithium metal anodes with nonaqueous electrolytes. Chem. Rev. *120*, 13312–13348. https://doi.org/10.1021/acs.chemrev.0c00275.

4. Cao, X., Ren, X., Zou, L., Engelhard, M.H., Huang, W., Wang, H., Matthews, B.E., Lee, H., Niu, C., Arey, B.W., et al. (2019). Monolithic solid–electrolyte interphases formed in fluorinated orthoformate-based electrolytes minimize Li depletion and pulverization. Nat. Energy *4*, 796–805. https://doi.org/10.1038/s41560-019-0464-5.

5. Shadike, Z., Lee, H., Borodin, O., Cao, X., Fan, X., Wang, X., Lin, R., Bak, S.-M., Ghose, S., Xu, K., et al. (2021). Identification of LiH and nanocrystalline LiF in the solid–electrolyte interphase of lithium metal anodes. Nat. Nanotechnol. *16*, 549–554. https://doi.org/10.1038/s41565-020-00845-5.

6. Li, Y., Huang, W., Li, Y., Pei, A., Boyle, D.T., and Cui, Y. (2018). Correlating structure and function of battery interphases at atomic resolution using cryoelectron microscopy. Joule *2*, 2167–2177. https://doi.org/10.1016/j.joule.2018.08.004.

7. Fan, X., Ji, X., Han, F., Yue, J., Chen, J., Chen, L., Deng, T., Jiang, J., and Wang, C. (2018). Fluorinated solid electrolyte interphase enables highly reversible solid-state Li metal battery. Sci. Adv. *4*, eaau9245. https://doi.org/10.1126/sciadv.aau9245.

8. Fan, X., Chen, L., Ji, X., Deng, T., Hou, S., Chen, J., Zheng, J., Wang, F., Jiang, J., Xu, K., and Wang, C. (2018). Highly fluorinated interphases enable high-voltage Li-metal batteries. Chem *4*, 174–185. https://doi.org/10.1016/j.chempr.2017.10.017.

9. Winter, M. (2009). The solid electrolyte interphase – the most important and the least understood solid electrolyte in rechargeable Li batteries. Z. Phys. Chem. *223*, 1395–1406. https://doi.org/10.1524/zpch.2009.6086.

10. Jiao, S., Ren, X., Cao, R., Engelhard, M.H., Liu, Y., Hu, D., Mei, D., Zheng, J., Zhao, W., Li, Q., et al. (2018). Stable cycling of high-voltage lithium metal batteries in ether electrolytes. Nat. Energy *3*, 739–746. https://doi.org/10.1038/s41560-018-0199-8.

11. Lin, D., Liu, Y., Li, Y., Li, Y., Pei, A., Xie, J., Huang, W., and Cui, Y. (2019). Fast galvanic lithium corrosion involving a Kirkendall-type mechanism. Nat. Chem. *11*, 382–389. https://doi.org/10.1038/s41557-018-0203-8.

12. Rustomji, C.S., Yang, Y., Kim, T.K., Mac, J., Kim, Y.J., Caldwell, E., Chung, H., and Meng, Y.S. (2017). Liquefied gas electrolytes for electrochemical energy storage devices. Science *356*, eaal4263. https://doi.org/10.1126/science.aal4263.

13. Weber, R., Genovese, M., Louli, A.J., Hames, S., Martin, C., Hill, I.G., and Dahn, J.R. (2019). Long cycle life and dendrite-free lithium morphology in anode-free lithium pouch cells enabled by a dual-salt liquid electrolyte. Nat. Energy *4*, 683–689. https://doi.org/10.1038/s41560-019-0428-9.

14. Markevich, E., Salitra, G., Chesneau, F., Schmidt, M., and Aurbach, D. (2017). Very stable lithium metal stripping–plating at a high rate and high areal capacity in fluoroethylene carbonate-based organic electrolyte solution. ACS Energy Lett. *2*, 1321–1326. https://doi.org/10.1021/acsenergylett.7b00300.

15. Luo, D., Zheng, L., Zhang, Z., Li, M., Chen, Z., Cui, R., Shen, Y., Li, G., Feng, R., Zhang, S., et al. (2021). Constructing multifunctional solid electrolyte interface via in-situ polymerization for dendrite-free and low N/P ratio lithium metal batteries. Nat. Commun. *12*, 186–211. https://doi.org/10.1038/s41467-020-20339-1.

16. Basile, A., Bhatt, A.I., and O'Mullane, A.P. (2016). Stabilizing lithium metal using ionic liquids for long-lived batteries. Nat. Commun. *7*. ncomms11794. https://doi.org/10.1038/ncomms11794.

17. Hope, M.A., Rinkel, B.L.D., Gunnarsdóttir, A.B., Märker, K., Menkin, S., Paul, S., Sergeyev, I.V., and Grey, C.P. (2020). Selective NMR observation of the SEI–metal interface by dynamic nuclear polarisation from lithium metal. Nat. Commun. *11*, 2224. https://doi.org/10.1038/s41467-020-16114-x.

18. Gunnarsdóttir, A.B., Amanchukwu, C.V., Menkin, S., and Grey, C.P. (2020). Noninvasive in situ NMR study of "dead lithium" formation and lithium corrosion in full-cell lithium metal batteries. J. Am. Chem. Soc. *142*, 20814–20827. https://doi.org/10.1021/jacs.0c10258.

19. Li, Y., Li, Y., Pei, A., Yan, K., Sun, Y., Wu, C.-L., Joubert, L.-M., Chin, R., Koh, A.L., Yu, Y., et al. (2017). Atomic structure of sensitive battery materials and interfaces revealed by cryo–electron microscopy. Science *358*, 506–510. https://doi.org/10.1126/science.aam6014.

20. Boyle, D.T., Huang, W., Wang, H., Li, Y., Chen, H., Yu, Z., Zhang, W., Bao, Z., and Cui, Y. (2021). Corrosion of lithium metal anodes during calendar ageing and its microscopic origins. Nat. Energy *6*, 487–494. https://doi.org/10.1038/s41560-021-00787-9.

21. Zachman, M.J., Tu, Z., Choudhury, S., Archer, L.A., and Kourkoutis, L.F. (2018). Cryo-STEM mapping of solid–liquid interfaces and dendrites in lithium-metal batteries. Nature *560*, 345–349. https://doi.org/10.1038/s41586-018-0397-3.

22. Han, B., Zhang, Z., Zou, Y., Xu, K., Xu, G., Wang, H., Meng, H., Deng, Y., Li, J., and Gu, M. (2021). Poor Stability of Li2CO3 in the solid electrolyte interphase of a lithium-metal anode revealed by cryo-electron microscopy. Adv. Mater. *33*, 2100404. https://doi.org/10.1002/adma.202100404.

23. Zhang, Z., Li, Y., Xu, R., Zhou, W., Li, Y., Oyakhire, S.T., Wu, Y., Xu, J., Wang, H., Yu, Z., et al. (2022). Capturing the swelling of solid-electrolyte interphase in lithium metal batteries. Science *375*, 66–70. https://doi.org/10.1126/science.abi8703.

24. Wang, X., Pawar, G., Li, Y., Ren, X., Zhang, M., Lu, B., Banerjee, A., Liu, P., Dufek, E.J., Zhang, J.-G., et al. (2020). Glassy Li metal anode for high-performance rechargeable Li batteries. Nat. Mater. *19*, 1339–1345. https://doi.org/10.1038/s41563-020-0729-1.

25. Lopez, J., Mackanic, D.G., Cui, Y., and Bao, Z. (2019). Designing polymers for advanced battery chemistries. Nat. Rev. Mater. *4*, 312–330. https://doi.org/10.1038/s41578-019-0103-6.

26. Aurbach, D., Youngman, O., and Dan, P. (1990). The electrochemical behavior of 1, 3-dioxolane—LiClO4 solutions—II. Contaminated solutions. Electrochim. Acta *35*, 639–655. https://doi.org/10.1016/0013-4686(90)87056-8.

27. Fang, C., Lau, J., Hubble, D., Khomein, P., Dailing, E.A., Liu, Y., and Liu, G. (2021). Large-molecule decomposition products of electrolytes and additives revealed by on-electrode chromatography and MALDI. Joule *5*, 415–428. https://doi.org/10.1016/j.joule.2020.12.012.

28. Qiu, F., Ren, S., Zhang, X., He, P., and Zhou, H. (2021). A high efficiency electrolyte enables robust inorganic–organic solid electrolyte interfaces for fast Li metal anode. Sci. Bull. *66*, 897–903. https://doi.org/10.1016/j.scib.2021.01.007.

29. Zhao, Q., Liu, X., Zheng, J., Deng, Y., Warren, A., Zhang, Q., and Archer, L. (2020). Designing electrolytes with polymerlike glass-forming properties and fast ion transport at low temperatures. Proc. Natl. Acad. Sci. USA *117*, 26053–26060. https://doi.org/10.1073/pnas.2004576117.

30. Zhao, Q., Liu, X., Stalin, S., Khan, K., and Archer, L.A. (2019). Solid-state polymer electrolytes with in-built fast interfacial transport for secondary lithium batteries. Nat. Energy *4*, 365–373. https://doi.org/10.1038/s41560-019-0349-7.

31. Gao, Y., Yan, Z., Gray, J.L., He, X., Wang, D., Chen, T., Huang, Q., Li, Y.C., Wang, H., Kim, S.H., et al. (2019). Polymer–inorganic solid–electrolyte interphase for stable lithium metal batteries under lean electrolyte conditions. Nat. Mater. *18*, 384–389. https://doi.org/10.1038/s41563-019-0305-8.

32. Liu, F.-Q., Wang, W.-P., Yin, Y.-X., Zhang, S.-F., Shi, J.-L., Wang, L., Zhang, X.-D., Zheng, Y., Zhou, J.-J., Li, L., and Guo, Y.-G. (2018). Upgrading traditional liquid electrolyte via in situ gelation for future lithium metal batteries. Sci. Adv. *4*, eaat5383. https://doi.org/10.1126/sciadv.aat5383.

33. Mackanic, D.G., Yan, X., Zhang, Q., Matsuhisa, N., Yu, Z., Jiang, Y., Manika, T., Lopez, J., Yan, H., Liu, K., et al. (2019). Decoupling of mechanical properties and ionic conductivity in supramolecular lithium ion conductors. Nat. Commun. *10*, 5384. https://doi.org/10.1038/s41467-019-13362-4.

34. Kobayashi, M., Okamoto, I., and Tadokoro, H. (1975). Crystal vibrations of poly-1, 3-dioxolane crystal form II and treatment of statistical errors due to uncertainties in the atomic positions. Spectrochim. Acta A. *31*, 1799–1812. https://doi.org/10.1016/0584-8539(75)80235-2.

35. Camacho-Forero, L.E., Smith, T.W., and Balbuena, P.B. (2017). Effects of high and low salt concentration in electrolytes at lithium–metal anode surfaces. J. Phys. Chem. C *121*, 182–194. https://doi.org/10.1021/acs.jpcc.6b10774.

36. Liu, Y., Yu, P., Wu, Y., Yang, H., Xie, M., Huai, L., Goddard, W.A., and Cheng, T. (2021). The DFT-ReaxFF hybrid reactive dynamics method with application to the reductive decomposition reaction of the TFSI and DOL electrolyte at a lithium–metal anode surface. J. Phys. Chem. Lett. *12*, 1300–1306. https://doi.org/10.1021/acs.jpclett.0c03720.

37. Gao, H., Li, Y., Guo, R., and Gallant, B.M. (2019). Controlling fluoride-forming reactions for improved rate capability in lithium-perfluorinated gas conversion batteries. Adv. Energy Mater. *9*, 1900393. https://doi.org/10.1002/aenm.201900393.

38. Fang, C., Li, J., Zhang, M., Zhang, Y., Yang, F., Lee, J.Z., Lee, M.-H., Alvarado, J., Schroeder, M.A., Yang, Y., et al. (2019). Quantifying inactive lithium in lithium metal batteries. Nature *572*, 511–515. https://doi.org/10.1038/s41586-019-1481-z.

39. Adams, B.D., Zheng, J., Ren, X., Xu, W., and Zhang, J. (2018). Accurate determination of coulombic efficiency for lithium metal anodes and lithium metal batteries. Adv. Energy Mater. *8*, 1702097. https://doi.org/10.1002/aenm.201702097.

40. Mastronarde, D.N. (2005). Automated electron microscope tomography using robust prediction of specimen movements. J. Struct. Biol. *152*, 36–51. https://doi.org/10.1016/j.jsb.2005.07.007.

41. Kremer, J.R., Mastronarde, D.N., and McIntosh, J.R. (1996). Computer visualization of three-dimensional image data using IMOD. J. Struct. Biol. *116*, 71–76. https://doi.org/10.1006/jsbi.1996.0013.

42. Pettersen, E.F., Goddard, T.D., Huang, C.C., Couch, G.S., Greenblatt, D.M., Meng, E.C., and Ferrin, T.E. (2004). UCSF Chimera—a visualization system for exploratory research and analysis. J. Comput. Chem. *25*, 1605–1612. https://doi.org/10.1002/jcc.20084.

43. Aurbach, D., Daroux, M.L., Faguy, P.W., and Yeager, E. (1988). Identification of surface films formed on lithium in dimethoxyethane and tetrahydrofuran solutions. J. Electrochem. Soc. *135*, 1863–1871. https://doi.org/10.1149/1.2096170.

44. Kresse, G., and Furthmüller, J. (1996). Efficient iterative schemes for ab initio total-energy calculations using a plane-wave basis set. Phys. Rev. B Condens. Matter *54*, 11169–11186. https://doi.org/10.1103/physrevb.54.11169.

45. Kresse, G., and Hafner, J. (1993). Ab initio molecular dynamics for liquid metals. Phys. Rev. B Condens. Matter *47*, 558–561. https://doi.org/10.1103/PhysRevB.47.558.

46. Xie, M., Wu, Y., Liu, Y., Yu, P., Jia, R., Goddard, W.A., and Cheng, T. (2021). Pathway of in situ polymerization of 1, 3-dioxolane in $LiPF_6$ electrolyte on Li metal anode. Mater. Mater. Today Energy *21*, 100730. https://doi.org/10.1016/j.mtener.2021.100730.

47. Becke, A.D. (1993). Density-functional thermochemistry. III. The role of exact exchange. J. Chem. Phys. *98*, 5648–5652. https://doi.org/10.1063/1.464913.

48. Grimme, S., Antony, J., Ehrlich, S., and Krieg, H. (2010). A consistent and accurate ab initio parametrization of density functional dispersion correction (DFT-D) for the 94 elements H-Pu. J. Chem. Phys. *132*, 154104. https://doi.org/10.1063/1.3382344.

49. Marenich, A.V., Cramer, C.J., and Truhlar, D.G. (2009). Universal solvation model based on solute electron density and on a continuum model of the solvent defined by the bulk dielectric constant and atomic surface tensions. J. Phys. Chem. B *113*, 6378–6396. https://doi.org/10.1021/jp810292n.

50. Casida, M.E., Jamorski, C., Casida, K.C., and Salahub, D.R. (1998). Molecular excitation energies to high-lying bound states from time-dependent density-functional response theory: characterization and correction of the time-dependent local density approximation ionization threshold. J. Chem. Phys. *108*, 4439–4449. https://doi.org/10.1063/1.475855.

51. Matsuzawa, N.N., Ishitani, A., Dixon, D.A., and Uda, T. (2001). Time-dependent density functional theory calculations of photoabsorption spectra in the vacuum ultraviolet region. J. Phys. Chem. A *105*, 4953–4962. https://doi.org/10.1021/jp003937v.

52. Frisch, M.J., Trucks, G.W., Schlegel, H.B., Scuseria, G.E., Robb, M.A., Cheeseman, J.R., Scalmani, G., Barone, V., Petersson, G.A., Nakatsuji, H., et al. (2016). Gaussian 16, Revision A.03 (Gaussian, Inc.).